國立臺灣大學理學院物理學研究所

碩士論文

Department of Physics

College of Science

National Taiwan University

Master Thesis

金奈米粒子飽和與反飽和散射的非線性分析與應用

Study of Saturable and Reverse Scattering in a Single Gold
Nanoparticle by Saturated Excitation Microscopy

李炫

Hsuan Lee

指導教授：朱士維 博士

Advisor: Shi-Wei Chu, Ph.D.

中華民國 103 年 6 月

June, 2014

誌謝

在這不長不短的碩士生涯中，最要感謝的是指導我的朱士維老師。不僅在研究上給予細心的指導與啟發，更常常與我們討論做事的態度與方法，使我們在實驗室內外的大小事都能開始思考與仔細觀察。還要感謝朱老師給予我許多的機會出國開會與短期研究的交換，前前後後共約十個月在國外四處學習及增廣視野，讓我的碩士經歷更加豐富。在台灣的研究合作方面，感謝林宮玄老師在實驗上給予的指導，及濟源在實驗上協助。感謝張之威老師的討論與建議，及其團隊在樣本上的設計和製作。感謝陳永芳老師在百忙之中願意來參與碩士口試的審查。

在實驗室方面，首先要感謝東榆及冠宇學長，細心的指導使我在一開始打下良好的基礎。發達、學侑、冠杰、國仁、美瑜、柏輔、哲維、運儒、庭英、冠郁及柏萱等前輩後進無論在實驗上或是心態上都是互相鼓勵的夥伴。

在日本共三次的交換研究中，我要特別感謝大阪大學的藤田克昌老師的指導，讓我在這期間可以完全專心在研究上。感謝山中真仁博士、桶谷亮介、米丸泰央、增井恭子博士在實驗上的幫忙。以及感謝在 LaSIE 的牛場翔太、馬越貴之、三野聰大、望月健太郎、大橋慶郎、渡辺梢、岡田昌也等人在生活上的照顧，使得這為期近八個月的回憶尤其珍貴。

最後要感謝我的家人在經濟上與心態上的支持與鼓勵，讓我無論在國內還是國外的研究都能放心地投入，而不致於擔心其他外在的事務，沒有他們就不會有今天的我。

中文摘要

電漿子在光學領域一直是非常熱門的研究之一，在極為前端的科學期刊常可以看到相關的文章；而在應用上也是非常的廣泛，例如在生醫影像，生物探測，及光開關都可以看到電漿子的涉足。由於非線性效應的發現，電漿子所產生的電磁場的強度與密度被更為提高，進而增廣了其應用性，但其在影像上的解析度提昇目前僅限於近場顯微術。遠場光學顯微鏡的解析度受繞射所限，一般只能達到約波長的一半。過去二十年中，發展了許多新穎的超解析顯微技術，主要利用螢光的開關或是飽和等非線性光學特性來達到超高解析度，然而螢光具有光漂白的問題，無法做長時間的觀察。近年來，近年來，金奈米粒子的飽和散射性質的發現讓電漿子學的應用更為推廣，也已經被證實能夠應用在其中一種超解析度顯微術，飽和激發顯微術上，進而達到超越光學繞射極限，且可以長時間產生穩定的散射訊號，不像螢光的影像訊號會在短時間內逐漸減弱。除了飽和散射以外，金奈米粒子的反飽和散射性質也在更強的激發光下被發現，而其在共軛焦顯微術上的影像卻跟一般的粒子影像有所差異：呈現一種同心圓而非單一圓形的影像，且外圈的影像寬度非常窄。如果此極窄的外圈可以跟中心訊號分開的話，將能進一步提昇光學影像的解析度，然而，此外圈的影像無法與中心影像以共軛焦顯微術分開。因此，此論文的主軸是希望將反飽和散射結合飽和激發顯微術，希望能抽取出外圈的非線性訊號以增進解析度。

在本論文中，將先從飽和與反飽和散射影像出發，並探討金奈米粒子的飽和激發影像對於不同激發光強度的變化做討論，最後跟理論計算和螢光的情況做比較。此實驗結果與分析方法顯現出經由飽和激發顯微術的訊號能比一般的共焦點

顯微術得到更多的非線性資訊，繼而能更精確地量測金奈米粒子的非線性曲線，而推測出金奈米粒子飽和散射性質。除此之外，也能經由該結果而選定適當的激發強度，獲得解析度比以前更佳的金奈米粒子影像。
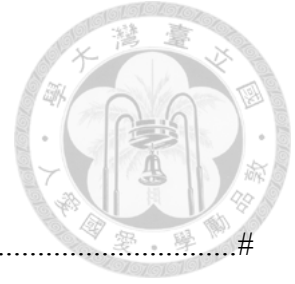
ABSTRACT
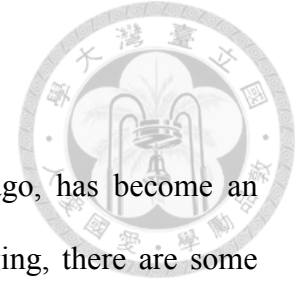
Optical microscopy, since its invention some 400 years ago, has become an essential tool in many disciplines. When considering optical imaging, there are some important factors, including contrast, resolution, magnification, imaging speed, penetration depth, noninvasiveness, etc. Among them, contrast is arguably the most important one. Without contrast, nothing can be observed no matter how good are other factors. During the last century, most of the major developments in optical microscopy are related to contrast, such as dark field, phase contrast, differential interference contrast, fluorescence, etc.

During last decade, there were significant breakthroughs in resolution of optical microscopy, relying on the nonlinearity of fluorescence. To avoid the photobleaching issue of fluorescence, we recently discovered saturable scattering in an isolated plasmonic particle, which can broaden the application of plasmonics in the fields of optical communication, sensing, and imaging. Combined with saturated excitation (SAX) microscopy technique, our discovery provides a new contrast agent for superresolution microscopy, with resolution down to $\lambda/8$. In addition, we also found that scattering from a single plasmonic particle exhibits reverse saturation behavior at higher excitation intensities, where very narrow side lobes and significantly reduced width of main lobe in the point spread function are observed, on a single particle basis. It will be very interesting to extract the reversed saturated part and to further enhance optical resolution by completely separating the side lobes from the main lobe. However, such separation is not possible with conventional confocal microscopy scheme. Here we explore the combination of reverse saturable scattering and SAX. With exerting modulated excitation light, the nonlinear signals can be extracted by Fourier transform
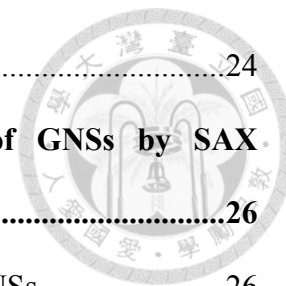
to realize SAX microscopy. Different from the SAX images of fluorescence, the nonlinear components of scattering show many dips at higher excitation intensity. Based on quantitative analysis of amplitude and phase of different frequency components in SAX, the phase change and resolution enhancement of signal are observed after every dip. The results suggest better resolution enhancement and higher signal contrast can be achieved by SAX microscopy in reverse saturable scattering region. The results can be used for achieving better resolution in imaging and investigating the nonlinear properties more precisely.

CONTENTS

Chapter 1   Introduction

1.1   Plasmonics

The study of plasmonics has attracted a lot of interests due to its applications in many different fields[1-4]. One of the most investigated fields among plasmonics is surface plasmon, which is the collective oscillation of conduction electrons coupling with an external electromagnetic wave at interface between metal and dielectric, and it has been explored for its potential in subwavelength optics, biophotonics, and microscopy[5-7]. The strong field enhancement in ultrasmall volume due to localized surface plasmon resonance (LSPR) in metallic nanoparticle has also attracted extensive attentions, not only because of its capability of boosting inherently weak nonlinear optical effects[8], but also its exceptional sensitivity to particle sizes, particle shapes, and dielectric properties of surrounding medium[9-12]. Its applications range from photonic integrated circuits to bio-sensing and near-field imaging techniques[2,3,13-15]. Fig. 1.1 shows the concept of LSPR, the ε_m and ε_d represent for dielectric constants of gold nanoparticle (GNP) and surrounding medium, respectively. It is worth to note that ε_m is strongly dependent with the wavelength of incident electric field due to the plasmonic resonance. The investigations of nonlinearity even broaden the applications due to its higher concentration of field[8].

However, such high nonlinearity and nano-scale size in imaging application is limited in the resolution enhancement of near-field microscopy[16], no far-field application of super-resolution based on plasmonics has been realized.
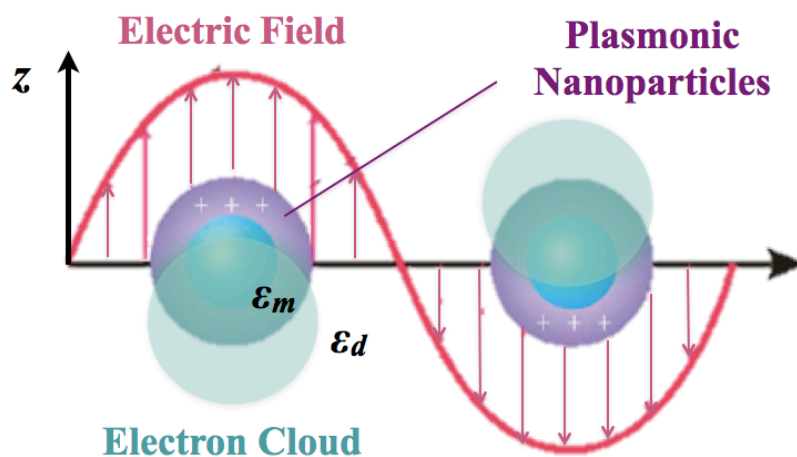
Fig. 1.1   Schematic diagram of the concept of LSPR.

1.2   Resolution on Optical Microscopy

Traditionally, far-field optical imaging is limited by diffraction of light; hence the optical resolution can only reach about half of light wavelength. During the last decade, such barrier was successfully overcome by manipulating the on/off switching of fluorophores[17-19], or by saturation of fluorescence emission[20-22], resulting in resolution below 100-nm. Nevertheless, fluorescence exhibits photobleaching issue, since the on/off switching techniques require repeated excitation of a fluorophore and the saturation techniques need strong incident power. Therefore, it will be more than desirable to develop super-resolution imaging modality based on an alternative contrast agent without bleaching, such as scattering.

One of the most appealing candidates is the extremely strong scattering from LSPR structure due to its strong field enhancement. And gold nanosphere (GNS) may be ideal as our main target, since the corresponding wavelength for LSPR is located in visible band.

1.3   Saturable and Reverse Saturable Scattering of Gold Nanoparticles

However, to our knowledge, neither switching nor saturation from LSPR structure has been reported, but nonlinearity of saturable absorption (SA)[23,24], that is, the absorption coefficient becomes smaller when the excitation intensity increases, in plasmonic nanoparticles embedded in a dielectric matrix has been widely studied. What's more, when the excitation intensity increases further, the absorption coefficient grows up again, showing the effect of reverse saturable absorption (RSA)[25,26]. The SA and RSA properties have applications on optical switching and all-optical signal processing[27,28]. Linked by Mie theory, scattering and absorption correlate with the real and imaginary parts of dielectric constant, it is therefore expected to see saturable scattering in a single plasmonic nanoparticle.

Recently, saturable scattering in an isolated plasmonic particle has been demonstrated for the first time[29]. In our daily life, it is common that the scattering response to excitation is linear; however, the demonstration shows that when the excitation intensity increases to a certain level, the nonlinearity of gold nanosphere (GNS) emerges and scattering intensity starts to saturate. The results also show saturable scattering has wavelength dependence, which may be related to LSPR. With the aid of SAX microscopy, superresolution based on saturable scattering is achieved. Overcoming the bleaching problem of fluorescence, the results of saturable scattering show great repeatability and reproducibility. The discovery of saturable shows great potential in superresolution microscopy, as a novel contrast agent without bleaching.

The scattering in GNS shows not only saturation, but also reverse saturation[30]. When the excitation intensity increases more after the scattering is saturated, the

scattering coefficient grows up again, showing the effect of reverse saturable scattering, similar to the effect of RSA, which once again suggests the possibility of shared mechanism between the nonlinear behaviors of scattering and absorption.

The saturable and reverse saturable scattering may be able to be explained by nonlinear optics. When the external electric field becomes strong enough, the response of material to electric field I_{out} is no longer linear; such nonlinear response can be described by input excitation intensity I_{in} in power series:

$$I_{out} = \alpha I_{in} + \beta I_{in}^2 + \gamma I_{in}^3 + ... \tag{1.1}$$

α is linear response coefficient; β and γ are nonlinear response coefficients of second and third orders, respectively

For lower light intensity, only the first term of Eq. (1.1) is important and the polarization coherently oscillates with the same frequency as input electric field. However, for strong excitation intensity, the higher-order ($n > 1$) terms of Eq. (1.1) are not negligible anymore. Radiations at sums or differences of the incident light frequencies will be observed. since the nonlinear absorption is not an instantaneous response (i.e. one or more transition processes may be involved)[28,31], the intensity equation describing the nonlinearity is at the average of time.

1.4   Super-resolution Microscopy with Gold Nanoparticles

With the aid of SAX microscopy, super-resolution based on saturable scattering has been achieved[29]. Overcoming the bleaching problem of fluorescence, the results of saturable scattering show great repeatability and reproducibility. In addition, scattering from a single plasmonic particle with reverse saturation shows very narrow side lobes and significantly reduced width of main lobe in the point spread function (PSF) are observed, on a single particle basis, as shown in Fig. 1.2. It will be very interesting to

extract the reversed saturated part and to further enhance optical resolution by completely separating the side lobes from the main lobe. However, such separation is not possible with conventional confocal microscopy scheme. Here we explore the combination of reverse saturable scattering and SAX. With exerting modulated excitation light, the nonlinear signals can be extracted by Fourier transform to realize SAX microscopy. Different from the SAX images of fluorescence, the nonlinear components of scattering show many dips at higher excitation intensity. Based on quantitative analysis of amplitude and phase of different frequency components in SAX, the phase change and resolution enhancement of signal are observed after every dip. The results suggest better resolution enhancement and higher signal contrast can be achieved by SAX microscopy in reverse saturable scattering region. The results can be used for achieving better resolution in imaging and investigating the nonlinear properties more precisely.
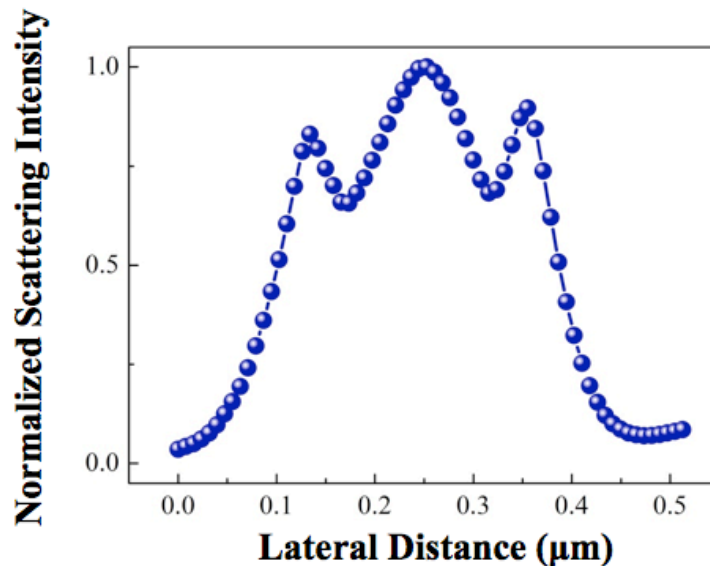

Fig. 1.2   Line profile of GNS with reverse saturable scattering. There's a very narrow

side lobe in the image.

Chapter 2   Theories

2.1   Extinction, Absorption, and Scattering of light by Small Gold Nanospheres

Under the assumption that the GNS behaves mainly as a dipole when illuminating by light, we can express the extinction coefficient and scattering coefficient from a single plasmonic nanoparticle according to Mie theory as[32,33]:

$$Q_{exc} = 4x\,\mathrm{Im}\left\{\frac{m^2-1}{m^2+2}\left[1+\frac{x^2}{15}\left(\frac{m^2-1}{m^2+2}\right)\frac{m^4+27m^2+38}{2m^2+3}\right]\right\}+\frac{8}{3}x^4\,\mathrm{Re}\left\{\left(\frac{m^2-1}{m^2+2}\right)^2\right\} \quad (2.1)$$

$$Q_{sca} = \frac{8}{3}x^4\left|\frac{m^2-1}{m^2+2}\right|^2 \quad (2.2)$$

Where x is $2\pi a/\lambda$, a is the radius of the sphere, and m^2 is $\varepsilon_m/\varepsilon_d$. By the simple relation that *Extinction = Absorption + Scattering*, the absorption coefficient can be determined as:

$$Q_{abs} = 4x\,\mathrm{Im}\left\{\frac{m^2-1}{m^2+2}\left[1+\frac{x^2}{15}\left(\frac{m^2-1}{m^2+2}\right)\frac{m^4+27m^2+38}{2m^2+3}\right]\right\} \quad (2.3)$$

With small x, the absorption is approximately:

$$Q_{abs} = 4x\,\mathrm{Im}\left\{\frac{m^2-1}{m^2+2}\right\} \quad (2.4)$$

By comparing equations (2.1) to (2.4), it is natural to see that the absorption and scattering of light by GNS are strongly correlated to each other. Therefore, when nonlinear behaviors such as saturable and reverse saturable absorption are observed, corresponding nonlinear phenomena for scattering can be expected. Further discussion will be made in the following contents.
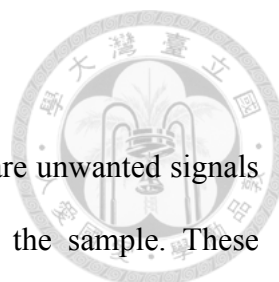
2.2   Confocal Laser Scanning Microscopy

In the conventional wide-field fluorescence microscope, there are unwanted signals from out-of-focus plane when the excitation light is focused on the sample. These unwanted signals would be collected with the signals at focus, and therefore causing high background and no resolution in depth.

To overcome this problem, confocal laser scanning microscopy (CLSM) was therefore invented in 1957, providing clear images at the focal plane on versatile applications[34-36]. Shown in Fig. 2.1, the basic concept is to place a confocal pinhole in front of a photodetector to block the signals that are out of objective lens focus; therefore only the wanted signal will be collected, showing the ability of optical sectioning. The confocal signals are acquired point by point by moving the focal point, and the images are reconstructed by a computer. With the in-focus signal from selected depth and laser scanning, we can obtain better-resolution optical images with optical sectioning.
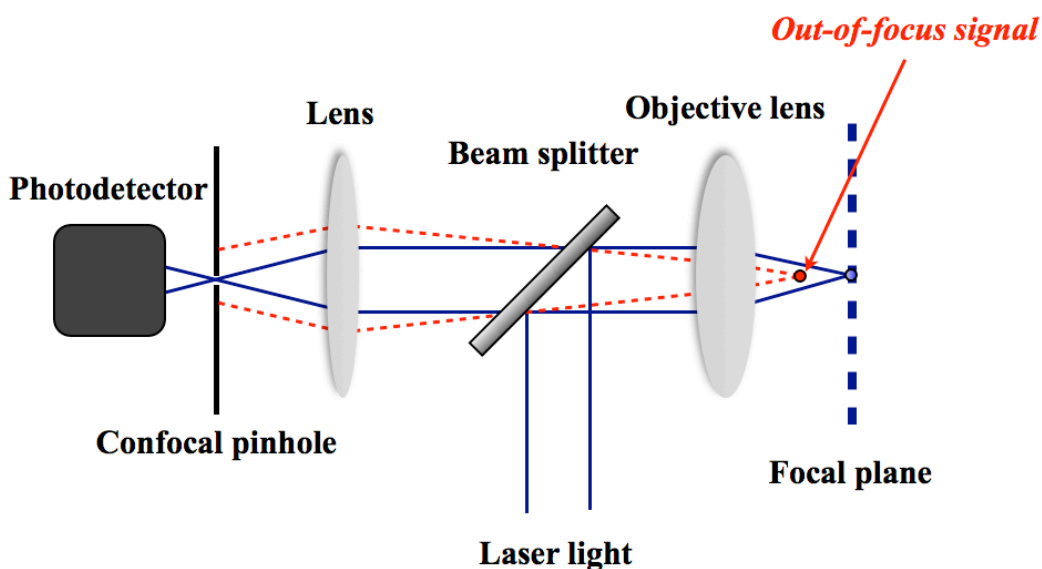

Fig. 2.1   Diagram of the concept of confocal microscopy.

When focusing a propagation light, the objective lens makes the light wave interference constructively at the point in space. Instead of focusing at an infinitesimal

point in ray optics, the focused light has specific volume due to diffraction limit in wave optics, and the focal point is also called point spread function (PSF). According to the works done by Ernst Abbe a hundred years ago, the lateral full width half maximum (R_{FWHM}) of PSF is:

$$R_{FWHM} \cong \frac{0.61 \times \lambda}{N.A.}$$ (2.5)

Where λ is wavelength of light and $N.A.$ is numerical aperture of the objective lens.

Since the CLSM images are reconstructed from point-by-point signals, the resulting images can be regarded as the convolution of PSF and sample. Because the size of PSF is limited, we cannot resolve two particles if their distance to each other is less than FWHM of PSF, which is also referred as the resolution of the microscope. In other words, the smaller effective PSF in the microscopy, the more details and information of objects

It is worth to note that what we can measure is the total power after objective lens; the exact peak intensity should be calculated from the Gaussian beam model. Since the peak scattering intensity from the center of PSFs:

$$I(r) = I_{max} e^{\frac{-2r^2}{w^2}}$$ (2.6)

Where r is the distance from center to position r, I_{max} is the intensity of the center of PSF and w is the radius where the intensity is (I_{max} e^{-2}). To connect the power and the peak excitation intensity after objective lens by the model, intensity of the whole space is integrated, as shown in below:
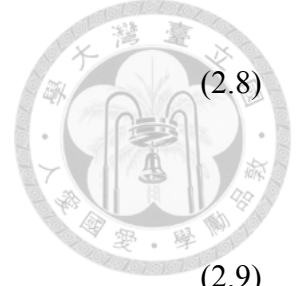
$$Power = \int_0^\infty I_{max} e^{\frac{-2r^2}{w^2}} dA = \frac{\pi}{2} \int_0^\infty I_{max} e^{\frac{-2r^2}{w^2}} r dr = \frac{\pi}{2} I_{max} w^2$$ (2.7)

Where *Power* is the total power after objective lens we can measure. By the definition of FWHM and (6.2.1), we can know the relation between FWHM and w:

$$w^2 = \frac{R_{FWHM}^2}{2\ln 2} \tag{2.8}$$

We can therefore acquire peak intensity $I_{\max}$ by

$$I_{\max} = (4\ln 2)\frac{Power}{\pi R_{FWHM}^2} \tag{2.9}$$

2.3 Saturated Excitation Microscopy

2.3.1 Concept of Saturation for Super-resolution

Because of the barrier of spatial resolution in optical microscopy, many superresolution techniques are therefore developed in the last two decades. Generally speaking, all of the superresolution methods are based on either switching[17-19], or saturation of fluorescence[20-22]. In this section, saturated excitation (SAX) microscopy based on the saturation of signals will be introduced, and applied as our main method for experiment.

The main idea of super-resolution imaging is to distinguish the signal at the center and outside of the focus. The resolution of optical microscopy is defined by the size of focus. If we can get the signals only from the center of focus, the equivalent focus size will be smaller, and therefore the resolution will become better. Since the excitation intensity at the center of focus is extremely high, and the one at outside of focus is much lower, the saturation of signals appears only at the former part and the signals at the later part shows linear response. We can successfully achieve better resolution if we are able to tell the saturation and linear response apart.

The method of SAX microscopy to make PSF narrower is to extract the saturated signal spatially, by applying temporal modulation of excitation light. As shown in Fig. 2.2, at the outside of PSF, the excitation intensity is not so strong, hence the response is linear to excitation, and there is only linear term of signal after Fourier transform.

However, at the center of PSF, the intensity is quite strong, the response shows saturation instead of linear, and after Fourier transform, the higher order harmonic signals in modulated frequency show up. With the aid of lock-in amplifier, we can selectively collect the signals in harmonic frequencies and reconstruct the image, and the effective PSF of it is reduced, achieving superresolution. Because we have to use a small focus for sampling and selectively get the saturation signals point-by-point, we cannot simply use wide field, but scanning.
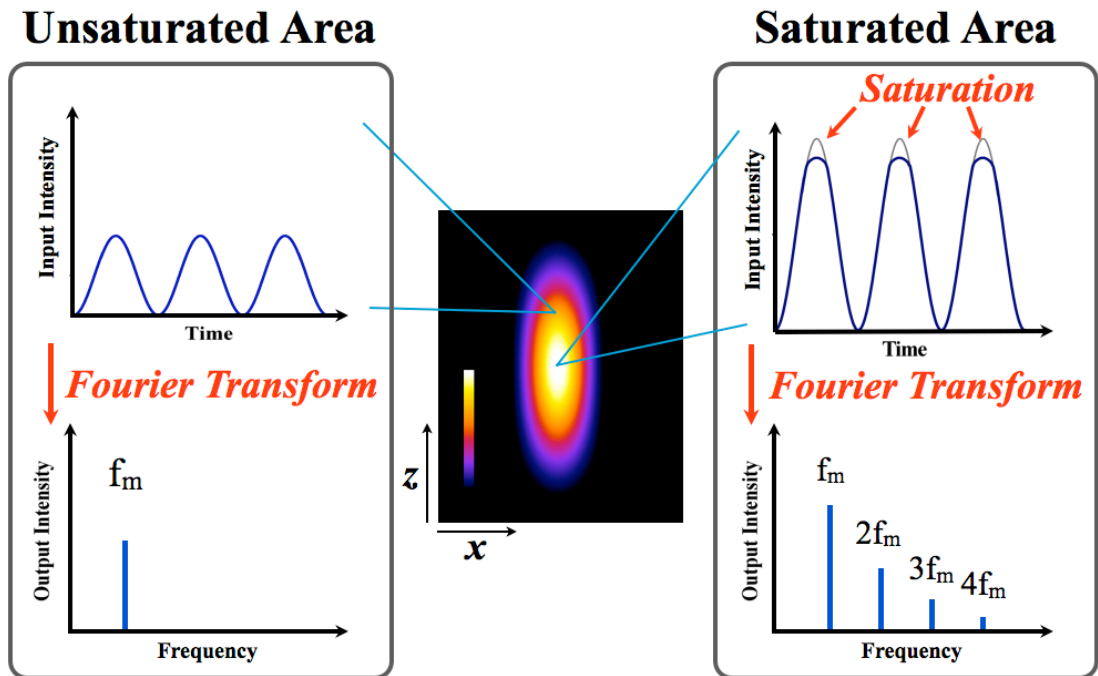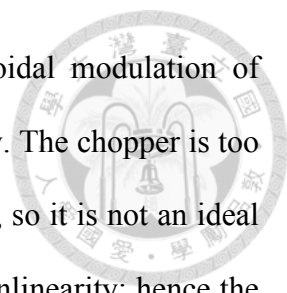
Fig. 2.2   Schematic diagram of the concept of SAX microscopy. The center image represents the PSF of focal point. The parts of two sides indicate the different responses of signals from different parts of PSF.

2.3.2   Generation of Modulation in Excitation Intensity

To generate temporal modulation of excitation intensity, modulators for excitation light are required. There are several kinds of way to generate intensity modulation, including chopper, modulation by some lasers, electro-optic modulator (EOM) and

acousto-optic modulator (AOM). Since the requirement of sinusoidal modulation of excitation intensity is critical, we have to choose modulator carefully. The chopper is too slow for imaging, and the modulation is in the form of square wave, so it is not an ideal candidate. The modulation from laser itself always includes high nonlinearity; hence the sinusoidal output is not ideal, either. With electro-optic effect, one EOM can only generate phase modulation, intensity modulation. And the intensity modulation from a single AOM cannot achieve good sinusoidal wave due to the imperfect linear response between first-order diffraction and the modulated voltage. For SAX microscopy, two AOMs are needed to generate temporal modulation of laser excitation intensity, from the beating of the small frequency difference between the two to achieve perfect sinusoidal wave.

The schematic diagram is shown in Fig. 2.3. The acoustic wave in the AO crystal is induced by electrical signals, resulting in the refractive index of the medium varies spatially and performs as an optical grating which diffracts the incident light and modulates its phase temporally.

Since the transmitted field is phase-modulated in time, a perfect sinusoidal modulated light is generated by constructive interference from overlapping two first-order transmitted fields spatially and temporally. The quality of the sinusoidal affects the signal-to-noise ratio of SAX images.

It is worthy to know that the peak intensity is twice of the I_{max} shown in Eq. (2.9) because of the sinusoidal modulation in intensity.
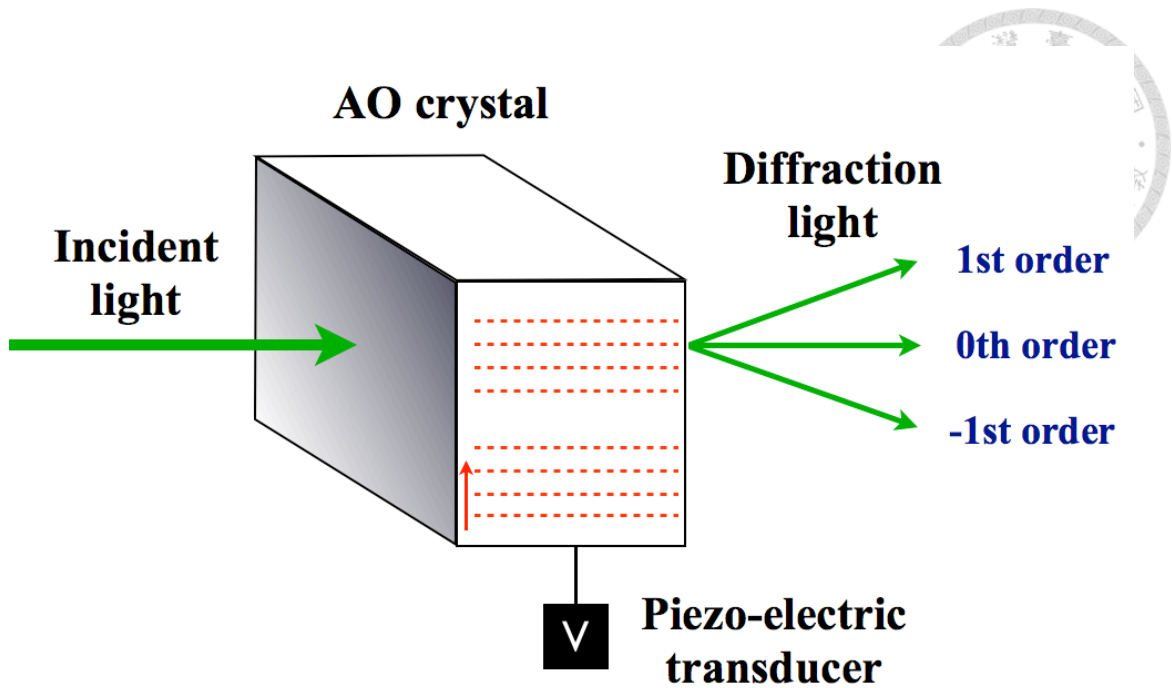
Fig. 2.3   Diagram of the concept of AOM by Raman-Nath scattering.

2.4   Method to Calculate SAX Signals

To further investigate the nonlinear behavior of SAX signals, calculation to connect the scattering and SAX signals of GNSs in different excitation intensities is required. The method is shown in the following steps:

1. Based on the fitting curve from experiment, first plot the curve of scattering signals versus excitation intensities, $S(I)$, as shown in Fig. 2.4(a).

2. Generate a intensity-modulated sinusoidal wave in time as excitation light, $I(t) = I(1+cos(2\pi f_m t))/2$, where f_m is the modulated frequency and I is the maximum intensity of the wave, as shown in Fig. 2.4(b).

3. Substitute the excitation into the scattering curve, i.e., $S(I(t))$, as shown in Fig. 2.4(c).

4. The same as the function of lock-in amplifier in experiment, we can acquire several terms of delta functions, like $\delta(f-f_m)$, $\delta(f-2f_m)$, $\delta(f-3f_m)$, and so on by Fourier transform of $S(I(t))$, where the f is the frequency after calculation. The coefficient of

each delta function represents its SAX signal.

5. By changing *I*, we can get the relationship between excitation intensity and SAX signals in different demodulated frequencies.
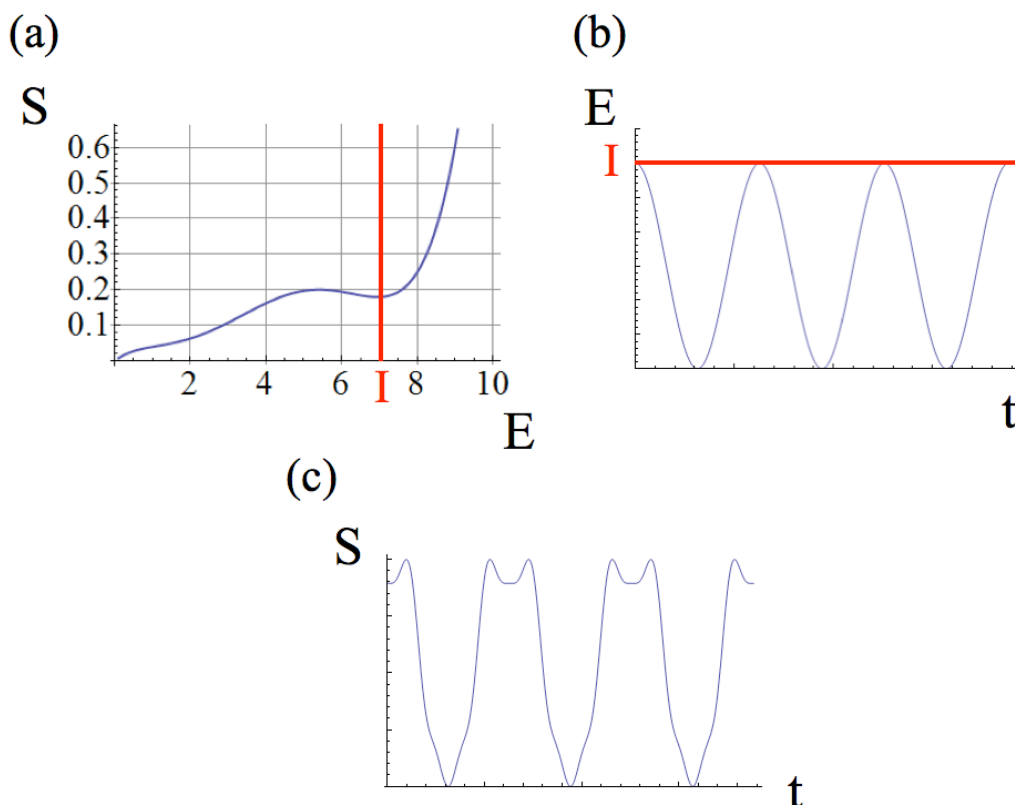
Fig. 2.4   (a) The polynomial fitting curve of scattering intensity to excitation intensity from experiment.

(b) The intensity-modulated sinusoidal curve in time as excitation light. The "I" indicates the maximum intensity of the curve.

(c) The curve after substitution between (a) and (b).

According to the reference of the original work of SAX microscopy, the calculation of fluorescence in SAX microscopy can be calculated from five-electronic-level system[37]. Since the rate constants in higher level is too small, we can actually calculate in a simpler model, three-electronic-level system[38], as shown in Fig. 2.5(a). The electrons in fluorophores absorb excitation light from ground state to

13

excited state, and emit fluorescent photons or go to the dark state; the relaxation time from dark state and the nonradiative decay are also counted into consideration, and more detailed calculation can be found in the reference. The fluorescence signal changing with excitation intensity is shown in Fig. 2.5(b) by calculation, showing saturation behavior of fluorescence when the excitation intensity is high. With the calculation method above, $1f_m$, $2f_m$, and $3f_m$ SAX signals changing with excitation intensity are shown in Fig. 2.5(c), showing only the flatten SAX signals when the excitation intensity is quite high. And the results are the same as the one in the first demonstration of fluorescence by SAX microscopy[22], proving the method of calculation above is correct.
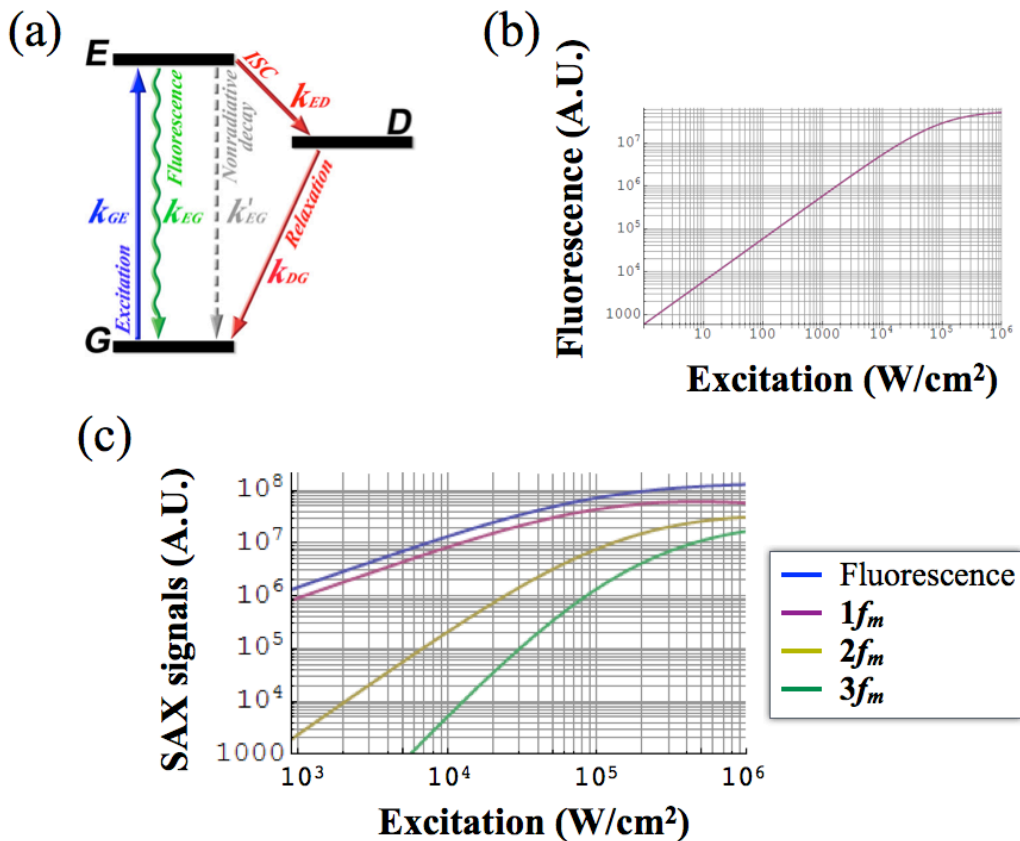

Fig. 2.5 (a) Energy diagram of fluorescence in three-electronic-level system. G represents the ground state; E represents the excited state; D represents the dark state. k_{GE}, k_{EG}, k^0_{EG}, k_{ED}, k_{DG} are the excitation rate constant, the

fluorescent rate constant, the nonradiative decay rate constant, the

intersystem crossing rate constant and the dark-state relaxation rate constant,

respectively[38].

(b) The curve of fluorescence signal to excitation intensity.

(c) The curves of $1f_m$, $2f_m$, and $3f_m$ SAX signals of fluorescence to excitation

intensity.

In fact, we can calculate the coefficients of $\delta(f\text{-}f_m)$, $\delta(f\text{-}2f_m)$ and $\delta(f\text{-}3f_m)$ separately if the signal curve can be expressed as polynomial, as the form in Eq. (1.1). If the $S(I)$ is expanded as a polynomial,

$$S(I) = \alpha I + \beta I^2 + \gamma I^3 + ... \tag{2.10}$$

where α, β, γ are linear, second-order, and third-order nonlinear constants, respectively. With the modulated excitation, $I(t) = I(1+cos(2\pi f_m t))/2$, the SAX signals can be calculated from Fourier transform,

$$F.T.[S(I(t))] = A_0\delta(f) + A_1\delta(f - f_m) + A_2\delta(f - 2f_m) + A_3\delta(f - 3f_m) + ... \tag{2.11}$$

where $F.T.[]$ is Fourier transformation, and A_1, A_2, and A_3 are the SAX signals for f_m, $2f_m$ and $3f_m$, respectively.

Since Fourier transform is a linear transformation, i.e.,

$$F.T.[af(t)] = a\{F.T.[f(t)]\} \tag{2.12}$$

where a is a constant, we can therefore get

$$F.T.[S(I)] = \alpha F.T.[I] + \beta F.T.[I^2] + \gamma F.T.[I^3] + ... \tag{2.13}$$

With the modulated excitation mentioned before,

$$F.T.[S(I(t))] = \alpha F.T.[I(t)] + \beta F.T.[I^2(t)] + \gamma F.T.[I^3(t)] + ... \tag{2.14}$$

And by calculation, we can easily get

$$F.T.[I(t)] = I\left\{\sqrt{\frac{\pi}{2}}\delta(f) + \frac{1}{2}\sqrt{\frac{\pi}{2}}[\delta(f - f_m) + \delta(f + f_m)]\right\} \qquad (2.15)$$

$$F.T.[I^2(t)] = I^2\left\{\frac{3}{4}\sqrt{\frac{\pi}{2}}\delta(f) + \frac{1}{2}\sqrt{\frac{\pi}{2}}[\delta(f - f_m) + \delta(f + f_m)] + \frac{1}{8}\sqrt{\frac{\pi}{2}}[\delta(f - 2f_m) + \delta(f + 2f_m)]\right\}$$

(2.16)

$$F.T.[I^3(t)] = I^3\left\{\begin{array}{l}\dfrac{5}{8}\sqrt{\dfrac{\pi}{2}}\delta(f) + \dfrac{15}{32}\sqrt{\dfrac{\pi}{2}}[\delta(f - f_m) + \delta(f + f_m)] + \dfrac{3}{16}\sqrt{\dfrac{\pi}{2}}[\delta(f - 2f_m) + \delta(f + 2f_m)] \\[2ex] + \dfrac{1}{32}\sqrt{\dfrac{\pi}{2}}[\delta(f - 3f_m) + \delta(f + 3f_m)]\end{array}\right\}$$

(2.17)

With the calculation above and ignore the components with plus frequency in delta functions (ex. $\delta(f+f_m)$), we can get the following relationship by comparison between the equations above

$$A_1 = \sqrt{\frac{\pi}{2}}(\frac{1}{2}\alpha I + \frac{1}{2}\beta I^2 + \frac{15}{32}\gamma I^3 + ...) \qquad (2.18)$$

$$A_2 = \sqrt{\frac{\pi}{2}}(\frac{1}{8}\beta I^2 + \frac{3}{16}\gamma I^3 + ...) \qquad (2.19)$$

$$A_3 = \sqrt{\frac{\pi}{2}}(\frac{1}{32}\gamma I^3 + ...) \qquad (2.20)$$

Hence once we get the α, β, γ, and so on from precise scattering curve, we can get the relationship between SAX signals and excitation intensity by calculation.

2.5 Calculation of SAX Signals from Reverse Saturable Scattering

To find out whether we can acquire the thin side lobe from reverse saturable scattering theoretically, we can calculate the SAX signals from the results in the

reference[30]. According to the reverse saturable scattering curve with third-order fitting, we can get the SAX signals in different excitation intensity by the method in Chapter 2.4, as shown in Fig. 2.6
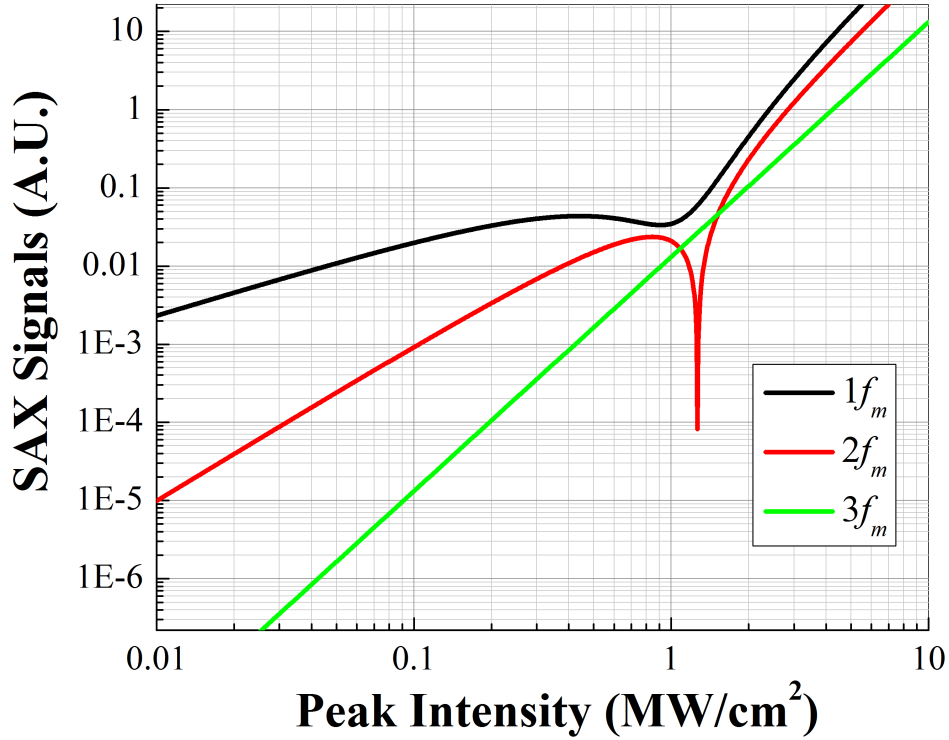

Fig. 2.6   Calculation of SAX signals by the reverse saturable scattering from reference[30].

With the calculation result in Fig. 2.6, we can see a clear dip in $2f_m$ signal at the excitation intensity around 1.2 MW/cm^2. The dip in $2f_m$ originates from Eq. (2.19) and the different signs of β and γ in the fitting curve, where the dip is expected when $2\gamma = -3\beta I$. With the dip of SAX signal, the extraction of side lobe is expected. Fig. 2.7 shows the calculated $2f_m$ image with 1.2 MW/cm^2 from the curve in Fig. 2.6. The result suggests the feasibility of the extraction of side lobe from reverse saturable scattering by SAX microscopy.
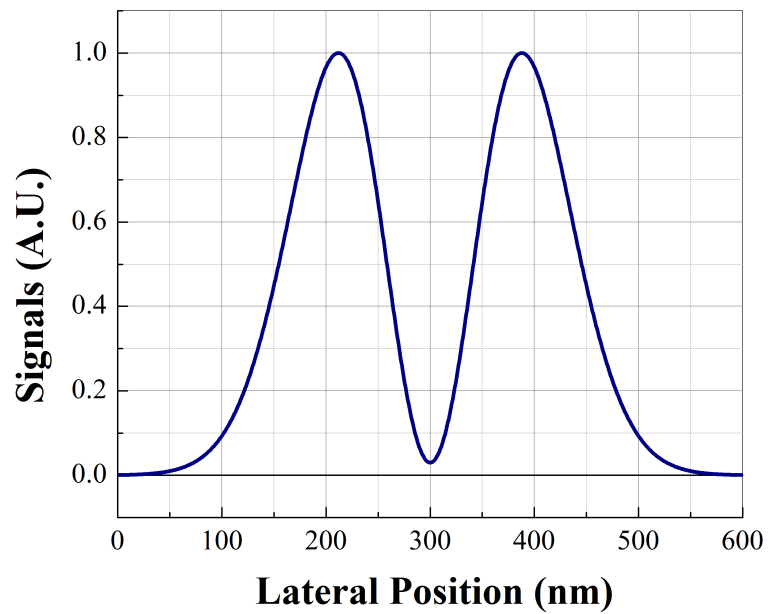
Fig. 2.6   Calculation of 2f$_m$ image at 1.2 MW/cm^2 from the curve in Fig. 2.7.

Another important issue of the dip in SAX signals is the slopes before and after it. The slope of the signal-to-excitation curve in log-log scale is related to the resolution in images. Fig 2.7(a) and (b) show the calculation results based on Eq. (2.5) with N.A 1.4 and 532-nm wavelength in Gaussian distribution. In Fig. 2.7(a), the calculation result shows the line profiles of PSFs with different slopes of the signal-to-excitation curve in log-log scale. When the slope is larger, the FWHM would be smaller. And Fig. 2.7(b) shows the resolutions of signals in different slopes. The resolution is enhanced when the slopes is larger.
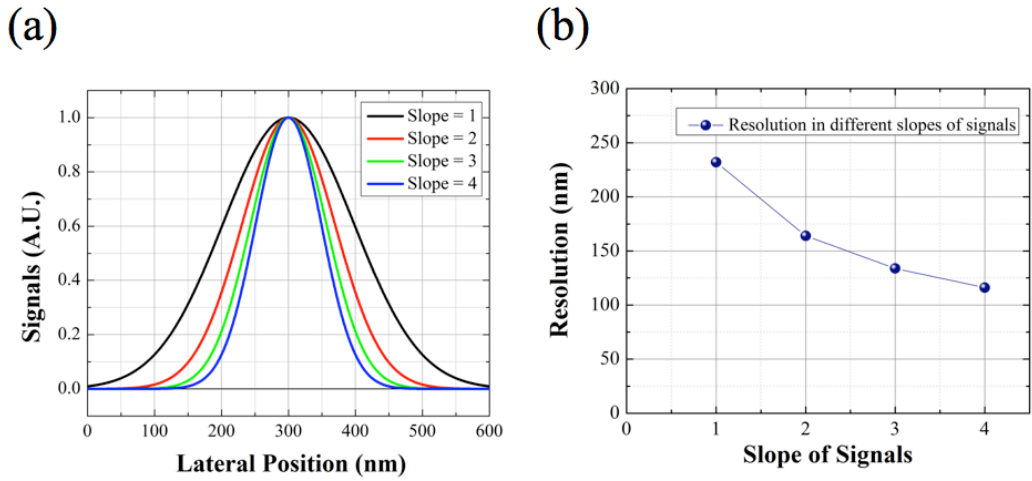
Fig. 2.7   (a) The line profiles of PSFs with different slopes of the signal-to-excitation

curve in log-log scale.

(b) The resolutions of signal in different slopes.

From Eq. (2.19), when the excitation intensity is low, the lower-order term, I^2 term, dominates $2f_m$ SAX signal. However, once the dip shows up, the higher order term, I^3 term, is comparable with the lower term, so the slope of $2f_m$ will be much closer to 3 when the I^3 term dominates after the dip. Therefore, the slope of $2f_m$ signal after the dip increases up to 3 in Fig. 2.6. Since the slopes of signals in log-log scale represent the resolution in images, the results indicate that the resolution of SAX images will increase after every dip.

Chapter 3   Experimental Setup and Sample

3.1   Experimental Setup

Our main target is 80-nm GNS whose plasmonic peak is around 570 nm. Shown in our previous results, the white light spectrum, which matches very well with the simulation spectrum by Mie theory. Due to the wavelength dependence of scattering saturation, we should choose closer laser wavelength to the resonance to get saturation easier.

Unlike z-scan technique which measures an ensemble of plasmonic particles embedded in dielectric media[25,26,39], optical microscopy can be used to measure the scattering signals from a single plasmonic particle to determine its optical properties. Fig. 3.1 shows the setup of a confocal microscope. With the aid of a standard reflection laser-scanning confocal microscope and an oil immersion objective lens with numerical aperture 1.4 (PlanApo, 100X, Olympus) for both excitation and collection, the scattering signals are detected by a photomultiplier tube (PMT) after a pinhole, and then the images are constructed by computer with synchronizing the PMT signal and scanning system, which is combined with a one-axis galvano mirror and a piezo stage (P-5613CD, Physik Instrumente) for two-dimensional imaging. The continuous-wave laser (EXLSR-532-300KH-W, Spectra-Physics Lasers) wavelength is chosen as 532 nm, which is close to the resonance peak of 80-nm GNS.

The more clear experiments of scattering curves and images are acquired in National Taiwan University. The oil immersion objective lens is numerical aperture 1.4 (UPlanApo, 100X, Olympus), and the two-axis scanning system including PMT is the commercial set named Fluoview 300 from Olympus. And continuous-wave laser wavelength is still chosen as 532 nm.
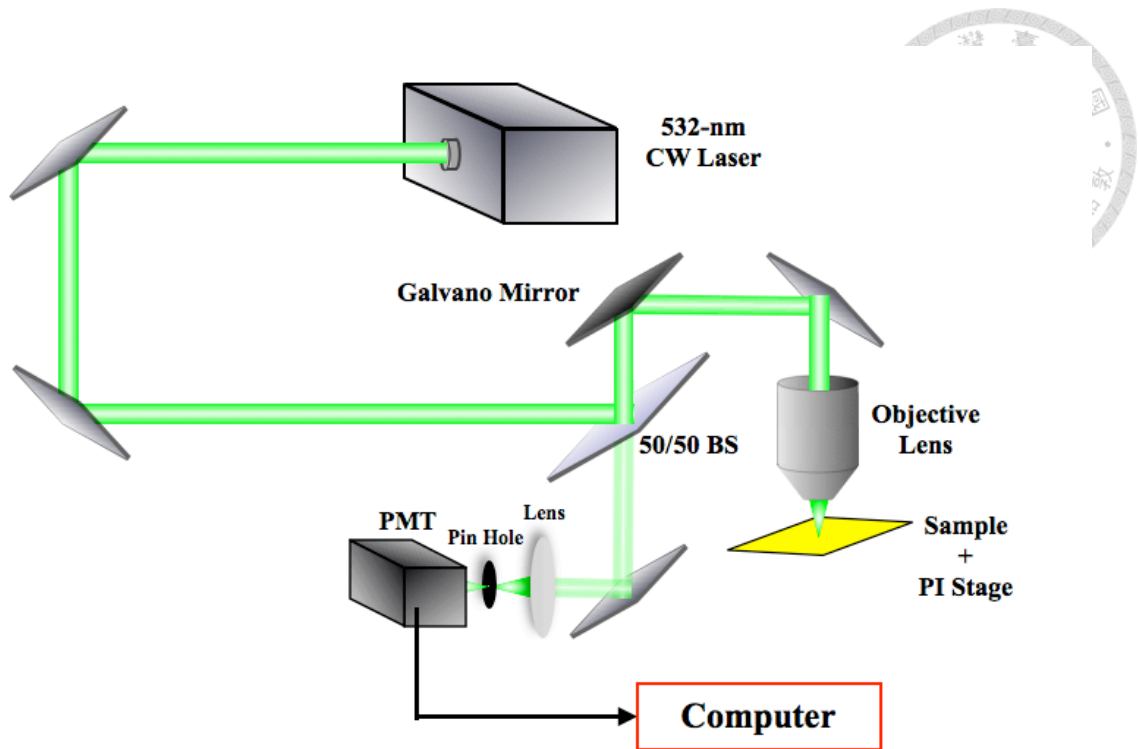
Fig. 3.1   The setup of confocal laser scanning microscopy for scattering measurement.

After ensuring the saturation phenomenon of scattering, we can achieve superresolution by SAX microscope, as shown in Fig. 3.2. The setup is constructed by Ryosuke Oketani in Osaka University. As mentioned in Chapter 2.3, one of the approaches to achieve better resolution is to extract the saturated region in a PSF of a single GNS. To generate an excitation source with temporally modulation, two AOMs (AOM-402AF1, IntraAction Corp.) are applied to reach almost 100% modulation depth, i.e. the lower bound intensity of sinusoidal modulation approaches zero. The modulation frequencies of the two AOMs are 40.00 and 40.01 MHz, respectively. By splitting the laser into two beams to pass through each AOM and recombining them together afterwards, modulation at beating frequency (10kHz) is obtained by a photon detector (PD), which is connected to a lock-in amplifier (HF2LI, Zurich Instrument) as the reference input. The modulated source goes through the same optical path of confocal microscope, and the signals from PMT are then sent to the lock-in amplifier to

extract signals in different harmonics of modulation frequencies. With synchronizing laser-scanning system, the different components of signals are finally sent to a computer to reconstruct two-dimensional scanning images. It is worthy to note that different harmonics frequencies after Fourier transform by lock-in amplifier are sent to the computer at the same time, in other words, $1f_m$, $2f_m$, and $3f_m$ images are acquired in parallel. In the normal cases, the higher order of modulated frequency image has the better optical resolution.
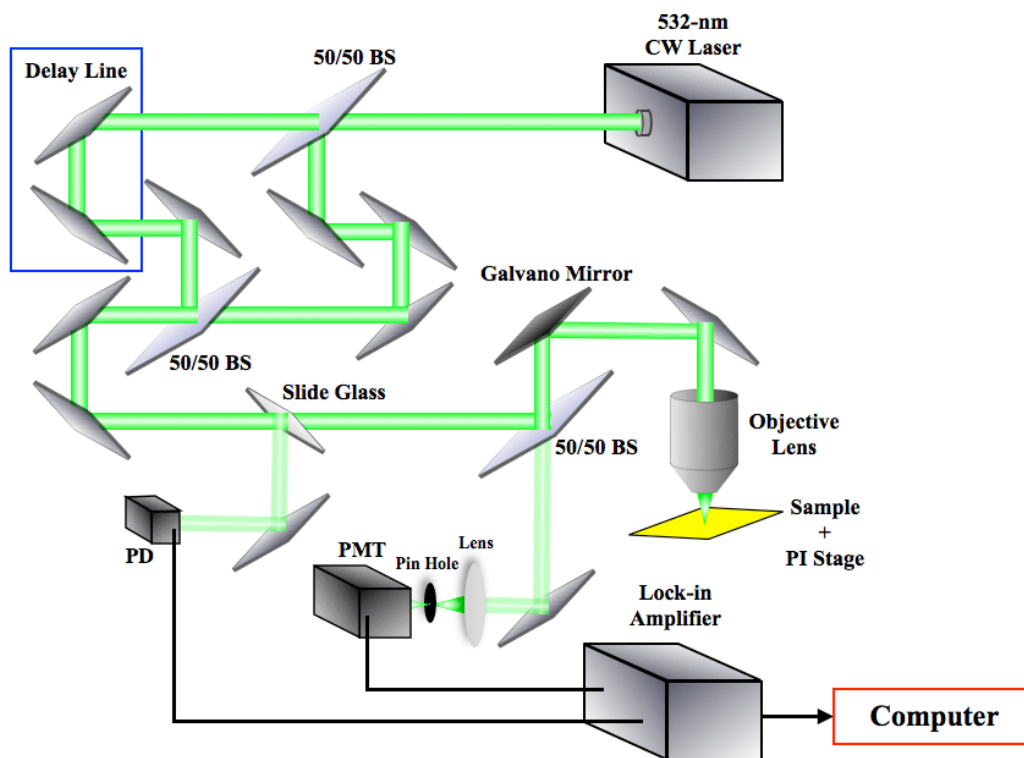

Fig. 3.2   The setup of SAX microscopy for scattering measurement.

3.2   Sample – Gold Nanospheres

3.2.1   Advantages of Gold Nanospheres

GNS is regarded as an ideal candidate to visualize the optical behaviors of gold material in nanometer scale because of the following advantages:

1.   Strong scattering due to LSPR

The scattering intensity is extremely strong if the excitation wavelength is close to the LSPR peak of GNS.

2. Polarization independent

Due to its circular geometry, GNS is polarization independent on excitation. Compared with other gold nanostructures, like gold nanorod or gold nanotriangle, the independent of GNS reduces the variables in the demonstration.

3. Chemical and physical stability

Compared with other plasmonics nanoparticles, GNS can resist high temperature compared with silver one, photo-irradiation, acids or oxidation[40].

4. Absorption band in visible wavelength range

The absorption peak of GNS changes with its size due to LSPR; the larger GNS size, the longer absorption wavelength. The absorption peaks of 40 - 100 nm GNSs range from 500 nm to 700 nm, which is easier for finding suitable laser and detection.

In this work, the GNSs are fabricated by British Biocell International with colloid chemical method[41]. The performance of their GNSs is qualified as high quality and features in over 400 million tests in the global market per year. The chosen diameters of commercial GNSs are 80 nm, whose scattering spectrum in oil is compared between the experimental measurement and calculation by Mie theory, as shown in Fig 3.3. The spectrum is measured by illuminating a wide wavelength range laser and collecting the backward scattering by a spectrometer (iDus 420, CCD DV420AOE, ANDOR). Both the experimental and calculation results are done by Yen-Ta Huang. The sizes and geometries of GNSs are also ensured by scanning electron microscope (SEM).
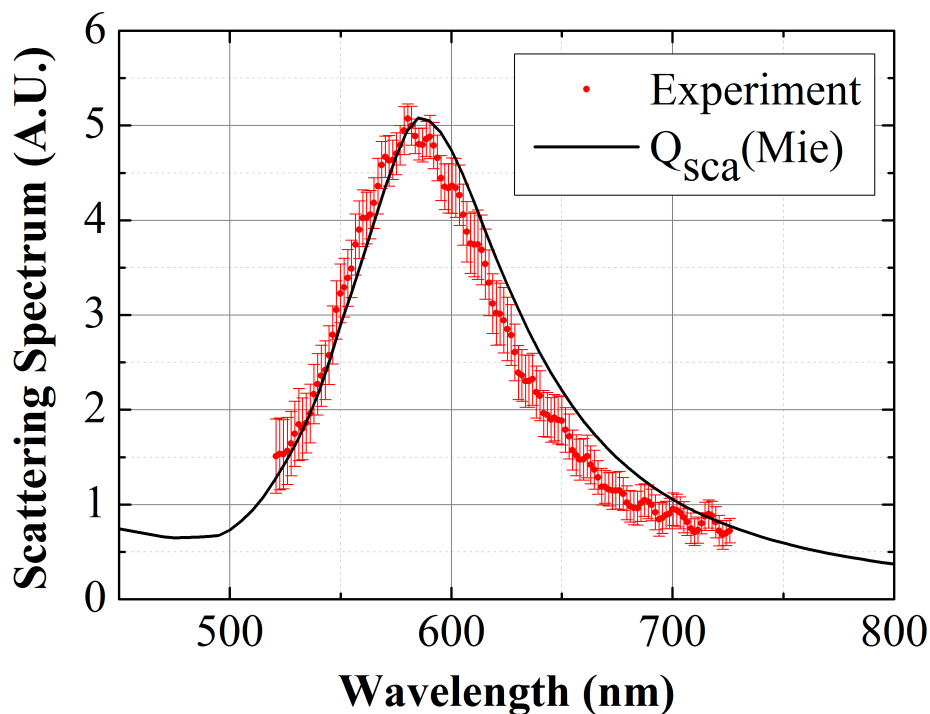
Fig. 3.3   The scattering spectrum of 80-nm GNS by experimental measurement (red

dots) and calculation by Mie theory (black line).

3.2.2   Sample Preparation for Microscopy

In order to measure the optical properties of GNSs, localization of them is crucial. To reach nonlinear regime of GNSs, the required excitation intensity is quite high, which results in the movements of particles and makes the measurement more difficult. The preparation procedures of GNSs sample for this experiment are listed as below:

1. Before preparation the sample, GNS colloid solution should be placed in ultrasonic cleaner for 15 minutes to prevent the aggregation of particles.

2. GNS colloid is dropped on a slide glass with magnesium aluminum silicate (MAS) coating to fix the GNSs.

3. After waiting for five to ten minutes, remove the extra colloid by distilled water to

prevent multi-layer GNSs.

4. Get rid of remaining distilled water by nitrogen gas.

5. To decrease the strong reflection from glass substrate, refractive index matching oil is added around GNSs.

6. Cover with cover glass and seal the sample by nail polish.

It is important to know that the attenuation spectra of GNSs in oil are different from the ones in water due to the change of dielectric constant of surrounding media. It is measured that the attenuations peaks of GNSs are red shifted for about 25 nm with immersion of oil.

Chapter 4 Saturable   and   Reverse   Saturable

Scattering of GNSs by SAX Microscopy

4.1   Saturable and Reverse Saturable Scattering of Isolated GNSs

By confocal laser scanning microscope, we can acquire scattering images in different excitation intensity. The range for linear response of PMT are measured, by the reflection of glass with changing input power, and the scattering intensity to PMT would be in the linear range by tuning neutral density (ND) filter appropriately. Even though there is additional photoluminescence signal from GNS while the excitation light is applied, the signal doesn't change obviously when the laser line filter is placed in front of PMT, indicating the photoluminescence signals is not comparable to scattering.

During the experiment, the darker GNSs in images are chosen, to prevent from acquiring the signals from the aggregating GNSs. By tuning the ND filter, we can control the excitation intensity for imaging. With the different scattering images of GNSs in different excitation intensity, the relationship between scattering intensity and excitation intensity is acquired.

To plot the scattering curve with excitation intensity, scattering signals at the center of the images, where the peak excitation intensity is highest, are selected. Four pixels for each image are averaged as a data point, to decrease the influence of noise from environmental fluctuation.

By getting the scattering value of the GNS center in images, we can plot the relationship between scattering intensity and excitation peak intensity, which is shown in Fig. 4.1. When the excitation intensity is less than 1.8×10^6 W/cm^2, the scattering

intensity is linearly dependent on the excitation. However, when the excitation increases over 1.8×10^6 W/cm², the scattering intensity goes away from linear (green line) obviously, showing the behavior of saturable scattering, in other words, scattering cross-section decreases dramatically. What's more, when the excitation intensity reaches 2.5×10^6 W/cm², the scattering cross-section quickly increases, showing reverse saturable scattering. However, there are more peaks occurring at even higher excitation intensity. Although the saturable and reverse saturable scattering is the focus, from Fig. 4.1, it is not difficult to understand that we can at least use fifth-order polynomial to fit the curve.
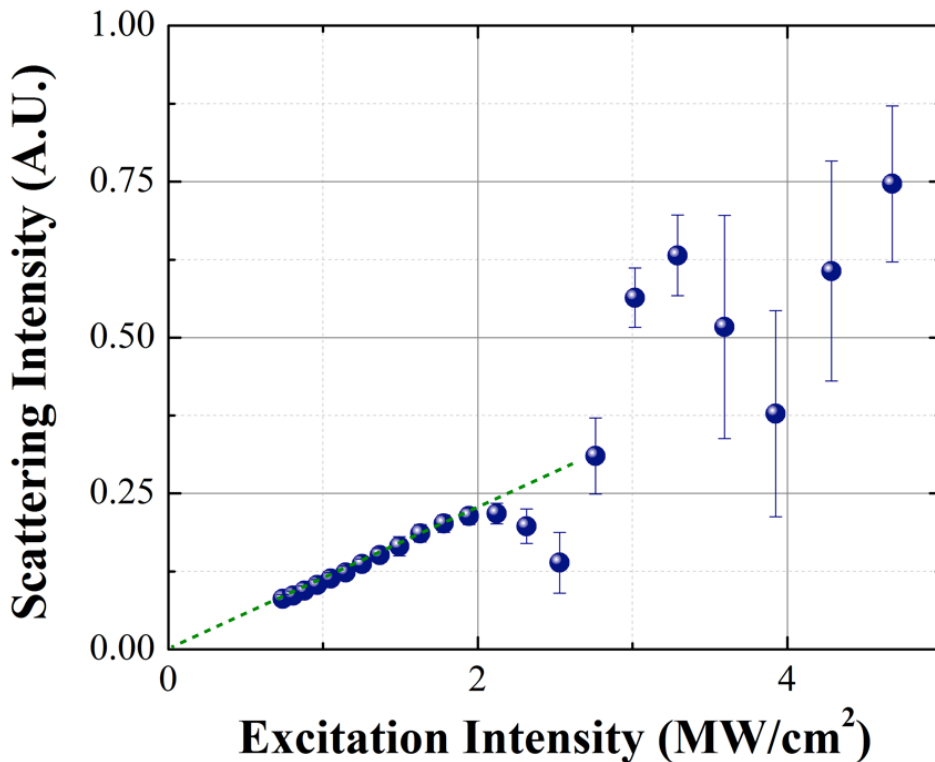

Fig. 4.1 The curve of scattering intensity to peak excitation intensity. Each data point is averaged from four 80-nm GNS, and the standard deviation of each point is also shown in the figure.

Since excitation intensities of the saturable and reverse saturable scattering of GNSs are very sensitive with different particles due to small inhomogeneous of sizes, only GNSs with similar geometry in images and turning point in intensity are selected for analysis. The scattering curve of saturation and reverse saturation is shown in Fig. 4.2, different from the data in Fig 4.1. It shows that saturable and reverse saturable scattering have great similarity to saturable and reverse saturable absorption, respectively. To further analyze the data, we introduce the similar way as these nonlinear behaviors of absorption, the nonlinearities of scattering intensity equation: $I_{sca} = \alpha I + \beta I^2 + \gamma I^3 + \delta I^4 + \varepsilon I^5 +$ higher-order terms, where I_{sca} and I are scattering intensity and excitation intensity, respectively; α is the linear scattering coefficient, and $\beta, \gamma, \delta,$ and ε are second, third, forth, and fifth order nonlinear coefficients, respectively. With the fitting curve (red line) in fifth-order polynomial, the signs of α, γ, and ε are positive, while the ones of β and δ are negative.
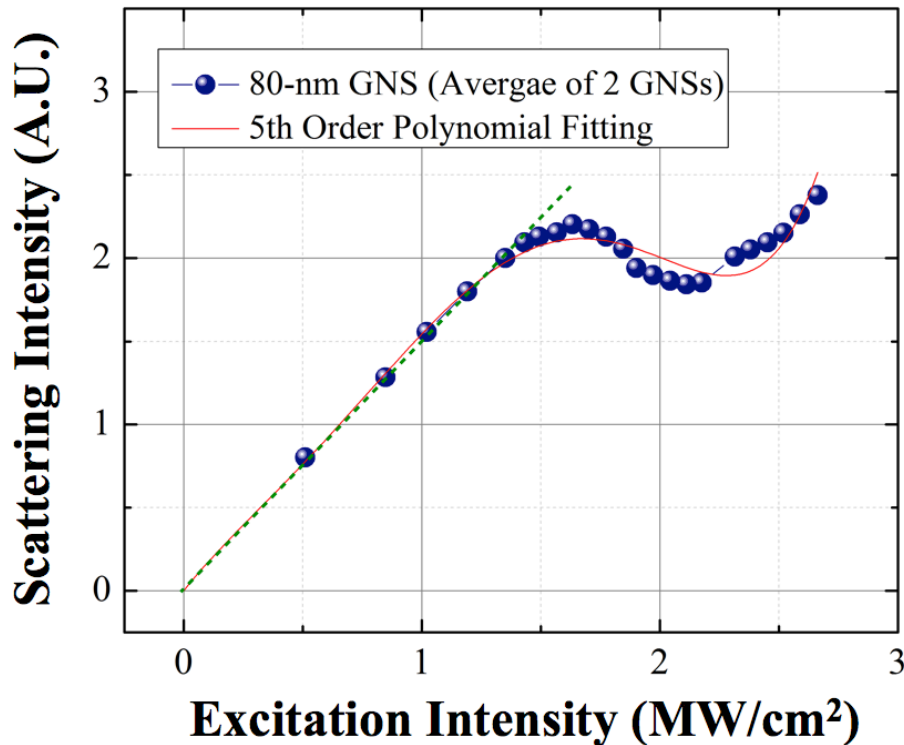

28

Fig. 4.2   The curve of scattering intensity to peak excitation intensity with saturation and reverse saturation. The red curve indicates the fitting of fifth-order polynomial.

Fig. 4.3 shows the scattering images under different excitation intensities. The pixel size is 13.8 nm, while each image size in Fig. 4.3 is 600 nm × 600 nm. Each image is averaged from 5 acquisitions to decrease the noise. The acquisition time is 234,000 pixels per second. In the linear region, the scattering intensity profile is a Gaussian function, just like excitation light. However, if we increase the excitation intensity up to 1.7×10^6 W/cm^2, and the FWHM is larger than in the linear region, showing the properties of saturation. We can clearly see the images evolve from linear, saturation, and reverse saturation with increasing excitation intensity. The results of the reverse saturable scattering exhibits ring shape in the scattering image.

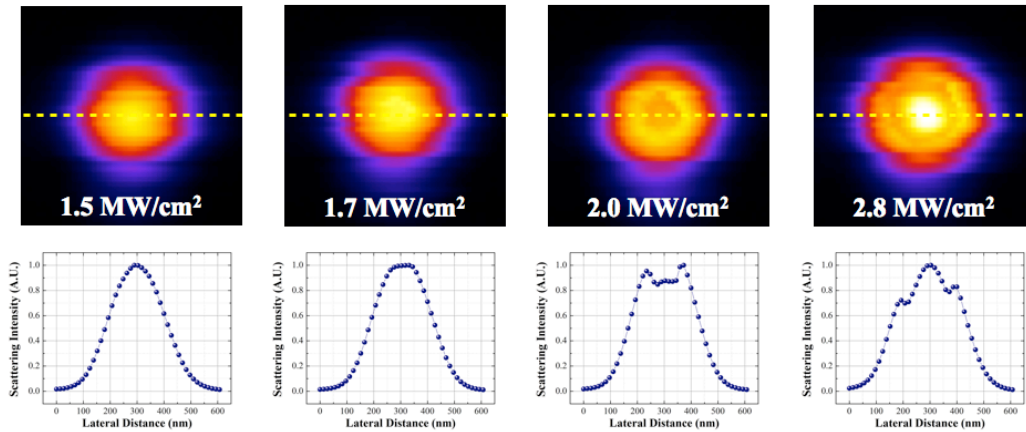*Fig. 4.3   The scattering images from linear, saturation, to reverse saturation region. The image size is 600 nm × 600 nm. The figures at bottom show the line profile of each image.*

It is obvious that the ring shape in the reverse saturable scattering image in Fig. 4.3 can be considered as the substitution of Gaussian beam and reverse saturation curve in Fig. 4.2, and the calculation is as shown in Fig. 4.4.
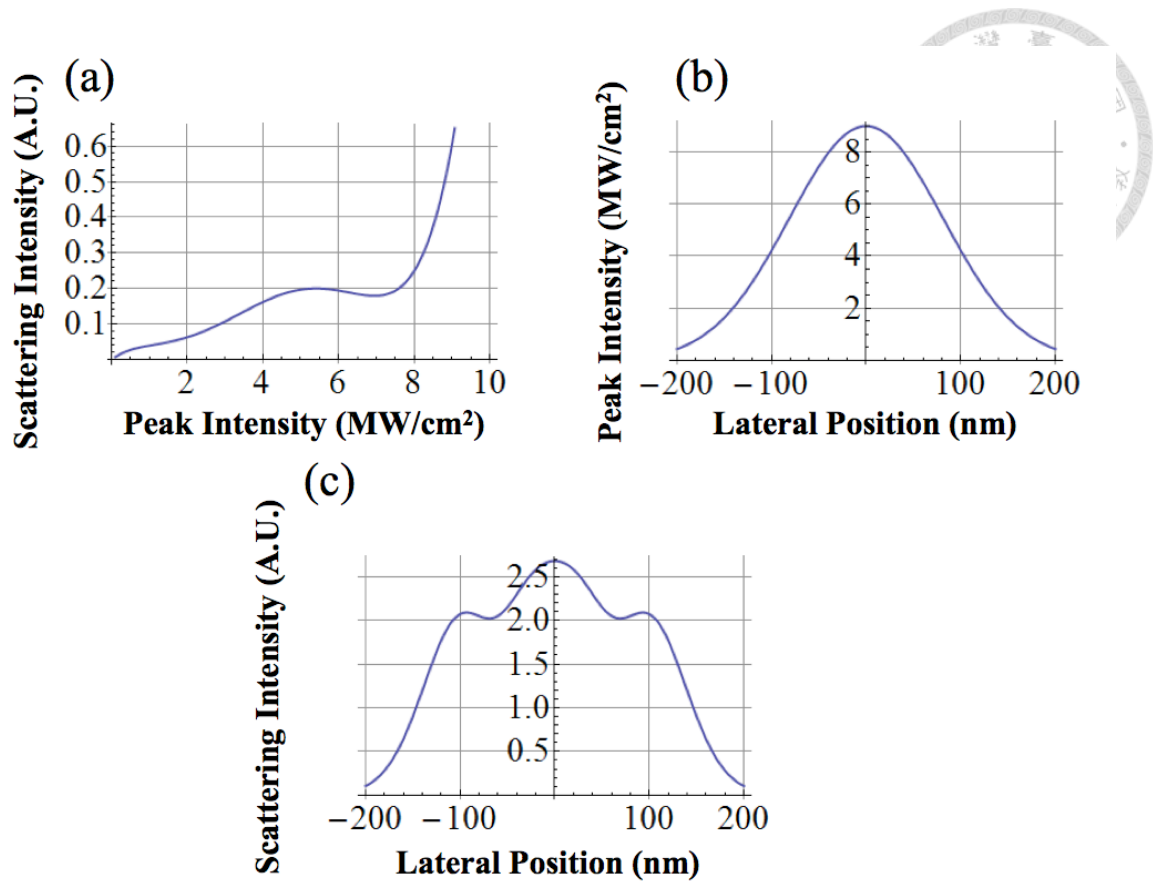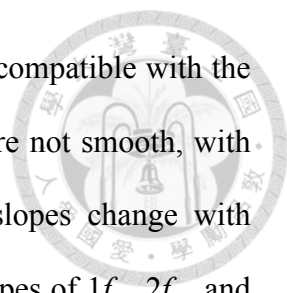
Fig. 4.4 (a) The scattering curve with reverse saturation.

(b) Excitation intensity with Gaussian distribution at focus.

(c) The substitution between (a) and (b), showing the scattering intensity in the line profile of an image.

4.2 Saturable and Reverse Saturable Scattering by SAX Microscopy

With the fitting curve of the result of saturation and reverse saturation of scattering in Fig. 4.2, now we can employ SAX technique to analyze the nonlinearity. Experimentally, the harmonic frequency components can be extracted by a lock-in amplifier, and the result is shown in Fig. 4.5(a). Fig. 4.5(b) shows the calculated result of A1, A2, and A3 in Eq. (2.18) to (2.20), corresponding very well to the experimental side.

From the result, there are two interesting observations that are compatible with the theoretical results in Chapter 2.5. First, the curves of $2f_m$ and $3f_m$ are not smooth, with some dips at specific intensities along the curves. Second, the slopes change with excitation intensity. When excitation intensity is not so high, the slopes of $1f_m$, $2f_m$, and $3f_m$ are 1, 2, and 3, respectively. However, after each dip, the slope becomes larger.

The first dip in $2f_m$ originates from Eq. (2.19) and the different signs of β and γ in the fitting curve, where the dip is expected when $2\gamma = -3\beta I$. If the intensity keeps increasing, another dip should occur when the contributions of nonlinear coefficients β, γ, and δ cancel out. Similarly, in the curve of $3f_m$ signals, the first dip is expected when the contributions of γ and δ cancel out.

Another important issue of the dip in SAX signals is the slopes before and after it. From Eq. (2.19), when the excitation intensity is low, the lower-order term, I^2 term, dominates $2f_m$ SAX signal. However, once the first dip shows up, the higher order term, I^3 term, is comparable with the lower term, so the slope of $2f_m$ will be much closer to 3 when the I^3 term dominates after the dip. The blue dot line in Fig. 4.5(a) shows the slope of $2f_m$ SAX signal becomes 3 after the first dip. For the same reason, after the first dip of $3f_m$ SAX signal and second dip of $2f_m$ SAX signal, the slopes of them become 4, as the purple dot lines in Fig. 4.5(a). Since the slopes of signals in log-log scale represent the resolution in images, the results indicate that the resolution of SAX images will increase after every dip.

In the calculation results, there are more dips at higher excitation intensity that are absent by experiment. It is due to the imperfection of fitting curve, thus more accurate and higher-order fitting is required.

(a)

Experiment
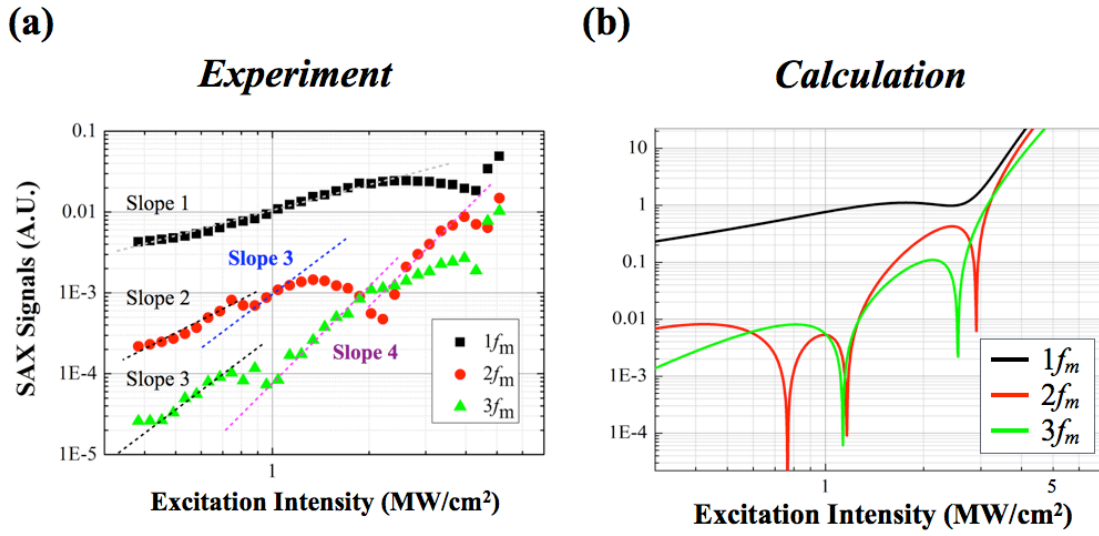

(b)

Calculation

Fig. 4.5　The curves of $1f_m$, $2f_m$, and $3f_m$ SAX signals to excitation intensities (a) by experiment and (b) calculation. Each data point is averaged from two 80-nm GNSs, and the standard deviation of each point is also shown in the figure. The dot lines in the figures indicate the slopes of each signal.

Since the peripheral of PSF is suppressed by this nonlinear dependence, the optical resolution is enhanced. Fig. 4.6(a) shows the SAX images in different excitation intensities. It is worthy to know that the images in Fig. 4.6(a) are the different sets of data from Fig. 4.5(a) due to the concerning of the image quality. When the excitation intensity is below 0.7 MW/cm^2, which is not so high, the slope of each SAX signal is normal (2 for $2f_m$, 3 for $3f_m$). Nevertheless, if we increase the excitation intensity up to the emergence of the dips of SAX signals, the SAX images change. For the excitation intensity around the first dip of $2f_m$, the $2f_m$ image shows donut geometry compared with Gaussian curve. When the excitation intensity increases up to the first dip of $3f_m$, only the $3f_m$ image shows a side lobe. All of the results of SAX images imply that the SAX signals that are away from the normal slopes do not result from noise, but from the SAX signal changes unquestionably.

The SAX images by calculation, which is from the curve in Fig. 4.5(b) are shown in Fig. 4.6(b) and 4.6(c), for comparison with the line profiles of experimental images at different geometry, corresponding with the normal Gaussian image, emergence of $2f_m$ and $3f_m$ donuts, respectively. In Fig. 4.6, the chosen intensities in calculation show similar properties to the curve of experiment. The images in Fig. 4.6(b) and 4.6(c) exhibit good match with the experiment. The experimental and calculation results suggest that the SAX image would show donut around dips. The side lobe in reverse saturable scattering can really be extracted by SAX microscopy.

It is worthy to note that in the reference of saturable scattering[29], the resolutions of $2f_m$ and $3f_m$ at lower excitation intensity is much better than theoretical prediction. The calculation method with slope in log-log scale cannot explain the extraordinarily great resolution of them. It is possibly because the nonlinear scattering is a coherent process, so that the convolution, which is used for incoherent process like fluorescence, is not suitable for calculating the resolution here.
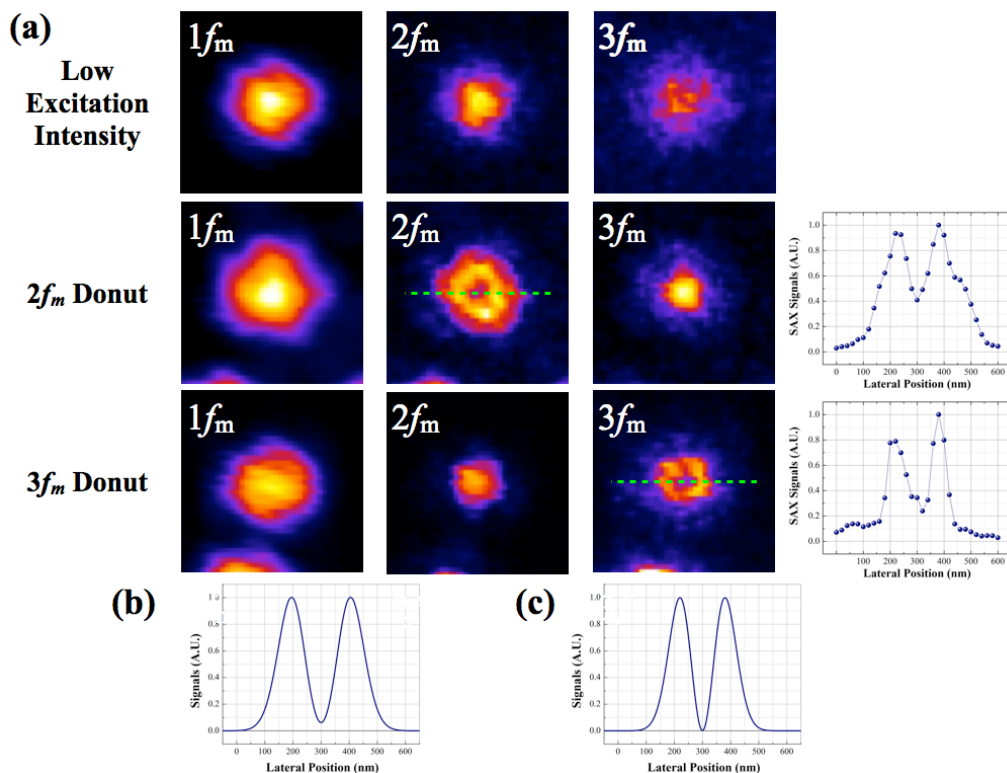
Fig. 4.6   SAX images in different excitation intensities by experiment and calculation. (a) The 1f$_m$, 2f$_m$, and 3f$_m$ SAX images at different excitation intensities by experiment. The pixel size is 20 nm, and each image size is 750 nm × 750 nm. The acquisition time is 1500 pixels per second. (b)-(c) The calculation results for comparison. (b) The 2f$_m$ image at 0.75 MW/cm^2 (c) The 3f$_m$ image at 1.1 MW/cm^2.

4.3   Phase of SAX signals

The dips of SAX signals imply that if we take the SAX images with the lock-in amplifier channel of output in "X" instead of "R", we may be able to see different signs of SAX signals before and after every dip.

To further verify the prediction, comparison between the SAX images of channel in "R" and "X" after a dip is needed. Fig. 4.7 shows the 2f$_m$ images by "R" and "X" channels while the peak excitation intensity is 8 MW/cm^2, which is higher enough to see multiple peaks clearly. By the "R" channel in Fig. 4.7, there are three clear peaks at the center, and two small peaks at two sides. However, by "X" channels, we can see the center peak of image shows different sign from the two clear peaks outside of it, the sign of two small peaks outside is also opposite to the two clear peaks. The result shows the origin of the dips in SAX signals is owing to the change of signs, and the signals by "X" channels may reveal the sign of each coefficient from scattering curve of GNSs. By differentiating the signs, we can simply acquire the signals from center peak.
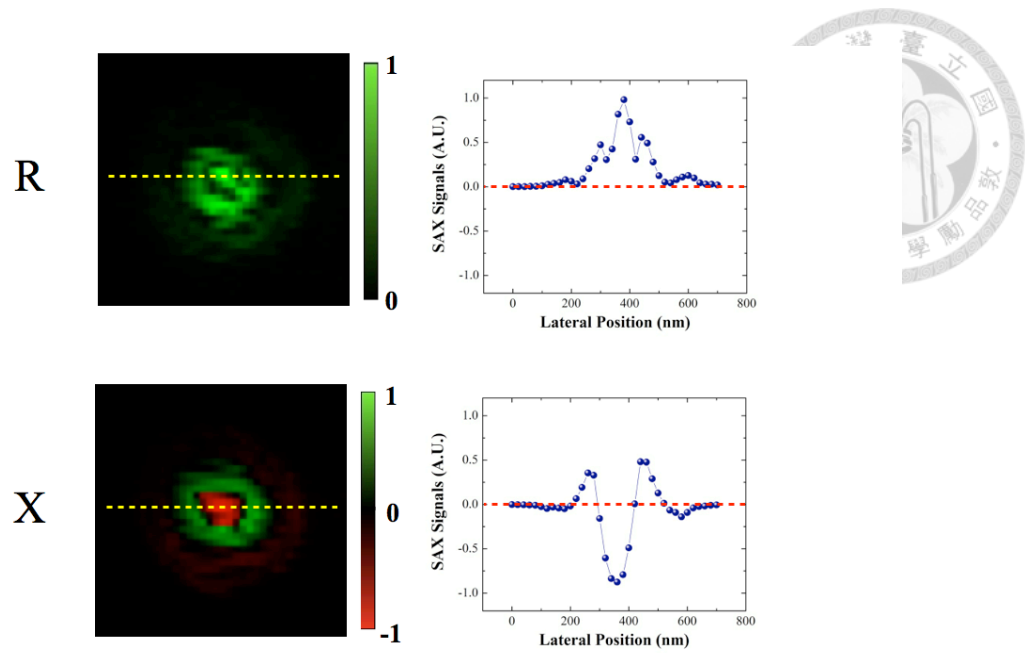
Fig. 4.7   The 2f$_m$ SAX images signal in "R" and "X" channels by lock-in amplifier, respectively.
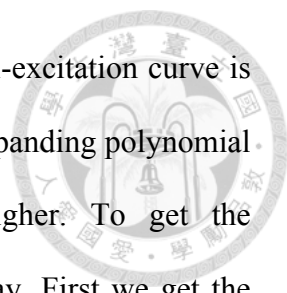
Chapter 5   Conclusions and future works

5.1   Conclusions

In conclusion, the combination of reverse saturable scattering and SAX is demonstrated. With exerting modulated excitation light, the nonlinear signals can be extracted by Fourier transform to realize SAX microscopy. Different from the SAX images of fluorescence, the nonlinear components of scattering show many dips at higher excitation intensity. Based on quantitative analysis of amplitude and phase of different frequency components in SAX, the phase change and resolution enhancement of signal are observed after every dip. The results suggest better resolution enhancement and higher signal contrast can be achieved by SAX microscopy in reverse saturable scattering region. The results can be used for achieving better resolution in imaging and investigating the nonlinear properties more precisely.

5.2   Future works

For the potential application from the experiment and calculation, we can get even higher slopes (in log-log scale) in $2f_m$ and $3f_m$ signals when the excitation intensity is higher compared with the case in lower one. With the aid of this different phenomenon of saturation in scattering, better resolution can be achieved in scattering than in fluorescence images by SAX microscopy. The $2f_m$ signals may have the same resolution enhancement as other higher order SAX signals, but with much higher signal-to-noise ratio, which is also a critical issue in SAX microscopy. What's more, if the excitation intensity is selected correctly, we can further get better resolution when the SAX signals arise from a drop, with extremely steep slope. The results can be applied for superresolution by the agents with high nonlinearity.
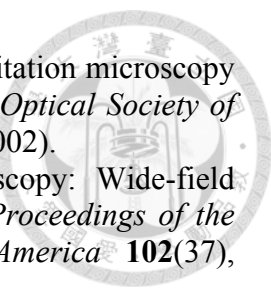
Another possible application by SAX analysis is to find the signal-excitation

relation more precisely. It is very common that the measured signal-excitation curve is not precise due to some noise or error, and the coefficients of the expanding polynomial are more incorrect when the order of the polynomial is higher. To get the signal-excitation curve, we can use the SAX method in reverse way. First we get the SAX signals of enough high order terms (ex. $6f_m$ or $7f_m$) by experiment from low to high excitation intensity, and it is not difficult to know that we can use every acquired term to do inverse Fourier transform, and further get scattering curve. The method can get even more precise curve because the drops at some specific excitation intensity show more information about the saturation. However, in experiment, higher order SAX signals imply lower signal-to-noise ratio; therefore high pass filter when getting higher order terms is required.

Reference

1. N. Fang, H. Lee, C. Sun, X. Zhang, "Sub-diffraction-limited optical imaging with a silver superlens," *Science* **308**(5721), 534-537 (2005).
2. B. Lee, S. Kim, H. Kim, Y. Lim, "The use of plasmonics in light beaming and focusing," *Progress in Quantum Electronics* **34**(2), 47-87 (2010).
3. S. Lal, S. Link, N.J. Halas, "Nano-optics from sensing to waveguiding," *Nature Photonics* **1**(11), 641-648 (2007).
4. S. Kawata, Y. Inouye, P. Verma, "Plasmonics for near-field nano-imaging and superlensing," *Nature Photonics* **3**(7), 388-394 (2009).
5. K. Kneipp, Y. Wang, H. Kneipp, L.T. Perelman, I. Itzkan, R. Dasari, M.S. Feld, "Single molecule detection using surface-enhanced Raman scattering (SERS)," *Physical Review Letters* **78**(9), 1667-1670 (1997).
6. S.M. Nie, S.R. Emery, "Probing single molecules and single nanoparticles by surface-enhanced Raman scattering," *Science* **275**(5303), 1102-1106 (1997).
7. J. Homola, S.S. Yee, G. Gauglitz, "Surface plasmon resonance sensors: review," *Sensors and Actuators B-Chemical* **54**(1-2), 3-15 (1999).
8. M. Kauranen, A.V. Zayats, "Nonlinear plasmonics," *Nature Photonics* **6**(11), 737-748 (2012).
9. F. Hache, D. Ricard, C. Flytzanis, "Optical nonlinearities of small metal particles - surface-mediated resonance and quantum size effects," *Journal of the Optical Society of America B-Optical Physics* **3**(12), 1647-1655 (1986).
10. B. Balamurugan, T. Maruyama, "Evidence of an enhanced interband absorption in Au nanoparticles: Size-dependent electronic structure and optical properties," *Applied Physics Letters* **87**(14), (2005).
11. S. Link, M.A. El-Sayed, "Size and temperature dependence of the plasmon absorption of colloidal gold nanoparticles," *Journal of Physical Chemistry B* **103**(21), 4212-4217 (1999).
12. K.L. Kelly, E. Coronado, L.L. Zhao, G.C. Schatz, "The optical properties of metal nanoparticles: The influence of size, shape, and dielectric environment," *Journal of Physical Chemistry B* **107**(3), 668-677 (2003).
13. J. Homola, "Present and future of surface plasmon resonance biosensors," *Analytical and Bioanalytical Chemistry* **377**(3), 528-539 (2003).
14. K.A. Willets, R.P. Van Duyne, Annual Review of Physical Chemistry, Annual Reviews, Palo Alto, 2007, pp. 267-297.
15. P.K. Jain, I.H. El-Sayed, M.A. El-Sayed, "Au nanoparticles target cancer," *Nano Today* **2**(1), 18-29 (2007).
16. B. Pettinger, B. Ren, G. Picardi, R. Schuster, G. Ertl, "Nanoscale probing of adsorbed species by tip-enhanced Raman spectroscopy," *Physical Review Letters* **92**(9), (2004).
17. E. Betzig, G.H. Patterson, R. Sougrat, O.W. Lindwasser, S. Olenych, J.S. Bonifacino, M.W. Davidson, J. Lippincott-Schwartz, H.F. Hess, "Imaging intracellular fluorescent proteins at nanometer resolution," *Science* **313**(5793), 1642-1645 (2006).
18. S.W. Hell, "Far-field optical nanoscopy," *Science* **316**(5828), 1153-1158 (2007).
19. B. Huang, W.Q. Wang, M. Bates, X.W. Zhuang, "Three-dimensional super-resolution imaging by stochastic optical reconstruction microscopy," *Science* **319**(5864), 810-813 (2008).

20. R. Heintzmann, T.M. Jovin, C. Cremer, "Saturated patterned excitation microscopy - a concept for optical resolution improvement," *Journal of the Optical Society of America a-Optics Image Science and Vision* **19**(8), 1599-1609 (2002).

21. M.G.L. Gustafsson, "Nonlinear structured-illumination microscopy: Wide-field fluorescence imaging with theoretically unlimited resolution," *Proceedings of the National Academy of Sciences of the United States of America* **102**(37), 13081-13086 (2005).

22. K. Fujita, M. Kobayashi, S. Kawano, M. Yamanaka, S. Kawata, "High-resolution confocal microscopy by saturated excitation of fluorescence," *Physical Review Letters* **99**(22), 228105 (2007).

23. L. De Boni, E.L. Wood, C. Toro, F.E. Hernandez, "Optical saturable absorption in gold nanoparticles," *Plasmonics* **3**(4), 171-176 (2008).

24. I. Ros, P. Schiavuta, V. Bello, G. Mattei, R. Bozio, "Femtosecond nonlinear absorption of gold nanoshells at surface plasmon resonance," *Physical Chemistry Chemical Physics* **12**(41), 13692-13698 (2010).

25. H.I. Elim, J. Yang, J.Y. Lee, J. Mi, W. Ji, "Observation of saturable and reverse-saturable absorption at longitudinal surface plasmon resonance in gold nanorods," *Applied Physics Letters* **88**(8), 083107 (2006).

26. U. Gurudas, E. Brooks, D.M. Bubb, S. Heiroth, T. Lippert, A. Wokaun, "Saturable and reverse saturable absorption in silver nanodots at 532 nm using picosecond laser pulses," *Journal of Applied Physics* **104**(7), (2008).

27. O. Wada, "Femtosecond all-optical devices for ultrafast communication and signal processing," *New Journal of Physics* **6**183 (2004).

28. N. Venkatram, R.S.S. Kumar, D.N. Rao, S.K. Medda, S. De, G. De, "Nonlinear optical absorption and switching properties of gold nanoparticle doped SiO2-TiO2 sol-gel films," *Journal of Nanoscience and Nanotechnology* **6**(7), 1990-1994 (2006).

29. S.W. Chu, T.Y. Su, R. Oketani, Y.T. Huang, H.Y. Wu, Y. Yonemaru, M. Yamanaka, H. Lee, G.Y. Zhuo, M.Y. Lee, S. Kawata, K. Fujita, "Measurement of a saturated emission of optical radiation from gold nanoparticles: application to an ultrahigh resolution microscope," *Physical Review Letters* **112**(1), 017402 (2014).

30. S.-W. Chu, H.-Y. Wu, Y.-T. Huang, T.-Y. Su, H. Lee, Y. Yonemaru, M. Yamanaka, R. Oketani, S. Kawata, S. Shoji, K. Fujita, "Saturation and reverse saturation of scattering in a single plasmonic nanoparticle," *ACS Photonics* **1**(1), 32-37 (2014).

31. D.D. Smith, Y. Yoon, R.W. Boyd, J.K. Campbell, L.A. Baker, R.M. Crooks, M. George, "Z-scan measurement of the nonlinear absorption of a thin gold film," *Journal of Applied Physics* **86**(11), 6200-6205 (1999).

32. G. Mie, "Articles on the optical characteristics of turbid tubes, especially colloidal metal solutions," *Annalen Der Physik* **25**(3), 377-445 (1908).

33. Z. Kam, "Absorption and scattering of light by small particles - BOHREN,C, HUFFMAN,DR," *Nature* **306**(5943), 625-625 (1983).

34. M. Rajadhyaksha, M. Grossman, D. Esterowitz, R.H. Webb, "In-vivo confocal scanning laser microscopy of human skin - melanin provides strong contrast," *Journal of Investigative Dermatology* **104**(6), 946-952 (1995).

35. A. Gruber, A. Drabenstedt, C. Tietz, L. Fleury, J. Wrachtrup, C. vonBorczyskowski, "Scanning confocal optical microscopy and magnetic resonance on single defect centers," *Science* **276**(5321), 2012-2014 (1997).

36. M. Rajadhyaksha, S. Gonzalez, J.M. Zavislan, R.R. Anderson, R.H. Webb, "In vivo confocal scanning laser microscopy of human skin II: Advances in instrumentation

and comparison with histology," *Journal of Investigative Dermatology* **113**(3), 293-303 (1999).

37. C. Eggeling, A. Volkmer, C.A.M. Seidel, "Molecular photobleaching kinetics of rhodamine 6G by one- and two-photon induced confocal fluorescence microscopy," *Chemphyschem* **6**(5), 791-804 (2005).

38. X.X. Zhu, W. Min, "Frequency-domain phase fluorometry in the presence of dark states: A numerical study," *Chemical Physics Letters* **516**(1-3), 40-44 (2011).

39. M.X. Ren, B.H. Jia, J.Y. Ou, E. Plum, J.F. Zhang, K.F. MacDonald, A.E. Nikolaenko, J.J. Xu, M. Gu, N.I. Zheludev, "Nanostructured plasmonic medium for terahertz bandwidth all-optical switching," *Advanced Materials* **23**(46), 5540-5544 (2011).

40. M.C. Daniel, D. Astruc, "Gold nanoparticles: Assembly, supramolecular chemistry, quantum-size-related properties, and applications toward biology, catalysis, and nanotechnology," *Chemical Reviews* **104**(1), 293-346 (2004).

41. G.F. Paciotti, L. Myer, D. Weinreich, D. Goia, N. Pavel, R.E. McLaughlin, L. Tamarkin, "Colloidal gold: A novel nanoparticle vector for tumor directed drug delivery," *Drug Delivery* **11**(3), 169-183 (2004).